Journal of The Electrochemical Society, **157** (5) E92-E97 (2010)
0013-4651/2010/157(5)/E92/6/$28.00 © The Electrochemical Society

Electrochemical Study on the Synthesis Process of Co–Ni Alloy Nanoparticles via Electroless Deposition

Shunsuke Yagi,*,z Makoto Kawamori, and Eiichiro Matsubara

Department of Materials Science and Engineering, Kyoto University, Kyoto 606-8501, Japan

The synthesis process of Co–Ni alloy nanoparticles via electroless deposition in ethylene glycol (EG) was electrochemically investigated. Insufficient thermodynamic data for organic solvents prevented us from calculating the oxidation–reduction (redox) potentials of Co(II)/Co and Ni(II)/Ni redox pairs in organic solvents. In the present work, however, the redox potentials of Co(II)/Co and Ni(II)/Ni redox pairs in EG were determined by using voltammetry combined with quartz crystal microbalance. In the cyclic voltammograms, the deposition current of cobalt on cobalt substrate was much higher than that of nickel on nickel substrate, which resulted in decreasing particle size with increasing nickel amount. Moreover, it was experimentally clarified that a mixed potential was determined by each partial reaction. Specifically, the hydrazine oxidation reaction was dominant in this reaction system, which is a key to controlling the mixed potential.
 [DOI: 10.1149/1.3352893]

Manuscript submitted December 22, 2009; revised manuscript received February 4, 2010. Published April 8, 2010.

Nanoparticles of iron group metals, i.e., Fe, Co, Ni, and their alloys, are attracting great interest because of their magnetic properties. Specifically, iron group alloy nanoparticles have high potential for various applications, such as magnetic field sensors, electronic inductors, magnetic separation, and biomedical applications, because the magnetic properties of alloy nanoparticles can be tailored to the applications by composition, structure, and size. For example, de Julian Fernández et al. reported that $Co_{80}Ni_{20}$ and $Co_{50}Ni_{50}$ nanoparticles show soft (low coercivity, high permeability) and hard (high coercivity) magnetic properties, respectively. Numerous synthesis processes of iron group alloy nanoparticles have been reported using hydrogen plasma–metal reaction,[1] thermal decomposition,[2] magnetron sputtering,[3] gas reduction in a biopolymer,[4] gas reduction combined with a sol–gel method,[5,6] polyol reduction,[7,8] and electroless deposition.[9,10] Electroless deposition using reducing agents is one of the most promising methods because nanoparticles with a wide variety of compositions can be obtained. Moreover, even the crystalline structure can be changed by the kind of reducing agent. For example, Vargas et al. reported that Co–Ni amorphous nanoparticles containing B can be obtained by using sodium borohydride ($NaBH_4$) as a reducing agent.[9]

We reported synthesis processes of copper,[11,12] cobalt,[13,14] nickel,[15] and tin[16] nanoparticles via electroless deposition. Additionally, we proposed the thermodynamical oxidation-state control of nanoparticles by comparing the mixed potential measured in the reaction solution with Pourbaix diagrams,[12,17] which is significantly effective in designing a synthesis process of nanoparticles in water. However, thermodynamic calculations cannot be easily adopted for reaction systems using organic solvents because of the lack of thermodynamic data in organic solvents. Against such a background, we determined the oxidation–reduction (redox) potential of the Co(II)/Co redox pair in ethylene glycol (EG) using voltammetry combined with a quartz crystal microbalance (QCM) and discussed the synthesis process of cobalt nanoparticles via electroless deposition.[18] In the present work, we further determined the redox potential of the Ni(II)/Ni redox pair in EG and investigated the synthesis process of Co–Ni alloy nanoparticles in EG. Moreover, it was experimentally clarified that the mixed potential is determined by each partial reaction, which is a key to controlling the mixed potential.

Experimental

Reaction solutions were prepared using reagent-grade cobalt chloride hexahydrate ($CoCl_2 \cdot 6H_2O$), nickel chloride hexahydrate ($NiCl_2 \cdot 6H_2O$), EG, sodium hydroxide (NaOH), hydrazine monohydrate ($N_2H_4 \cdot H_2O$), and chloroplatinic acid hexahydrate ($H_2PtCl_6 \cdot 6H_2O$) (Nacalai Tesque, Inc.) all as received. Reactions were conducted in a Pyrex beaker (100 cm^3 in capacity) by the following procedure. First, 27 cm^3 of EG solution containing 0.10 M metallic salts ($[CoCl_2] + [NiCl_2] = 0.10$ M) and 1.4 M NaOH was prepared, where M means mol dm^{-3}. Co(II) and Ni(II) ions in the metallic salt solution were hydroxylated to form green Co(II) and Ni(II) hydroxide sol. The nucleating agent $H_2PtCl_6 \cdot 6H_2O$ (2.0 mM) was added for experiments with the nucleating agent. Meanwhile, 27 cm^3 of EG solution containing 1.0 M N_2H_4 and 0.6 M NaOH was prepared. The temperature of the solutions was kept at a reaction temperature of 353 K in a water bath with nitrogen gas bubbling (50 cm^3 min^{-1}), starting at 30 min before the reaction and lasting throughout the reaction, to eliminate the effect of dissolved oxygen. The solutions were agitated at a rate of 500 rpm with a magnetic stirring unit. The metallic salt solution and the N_2H_4 solution were mixed at 353 K to start the reaction. The total amount of the reaction suspension was 54 cm^3, and thus the reaction EG suspension contained 0.50 M N_2H_4, 0.050 M metallic salts, 1.0 M NaOH, and 0 or 1.0 mM H_2PtCl_6. The crystalline structure of precipitates was investigated by an X-ray diffractometer (XRD, MAC Science Co., Ltd., M03XHF22) using a chromium X-ray tube. The morphology of precipitates was observed using a field-emission-scanning electron microscope (JEOL Ltd., JSM-6500F). The mean diameter and size distribution of the particles were determined by image analysis for 600 particles in each sample. The composition of nanoparticles was analyzed with energy-dispersive X-ray (EDX) spectrometry.

The deposition behavior of cobalt and nickel in EG was investigated in situ by QCM using circular 9 MHz AT-cut quartz crystal substrates, on both sides of which gold or nickel layers with a diameter of 5.0 mm were sputtered with an underlying titanium buffer layer. The QCM substrate was fixed inside a dipping-type Teflon holder (Seiko EG&G QCA917-21). The electrochemically active area of the QCM substrate was 0.196 cm^2. The holder with an oscillating circuit was connected to a frequency counter (Seiko EG&G QCA917) with a coaxial cable. The weight of cobalt deposited on the QCM substrate, Δm, was calculated from the change in resonance frequency of the QCM substrate, Δf (<0), by the Sauerbrey equation

$$-\Delta f = \frac{2f_0^2 \Delta m}{A\sqrt{\rho_q \mu_q}} \quad [1]$$

where f_0 is the frequency of the QCM substrate before the deposition, A is the active area of the QCM substrate (0.196 cm^2), ρ_q is the density of quartz (2.648 g cm^{-3}), and μ_q is the shear modulus of quartz (2.947×10^{11} g cm^{-1} s^{-2}). The immersion potential of the gold-sputtered QCM substrate was measured during several ex-

* Electrochemical Society Active Member.
z E-mail: syagi@mtl.kyoto-u.ac.jp

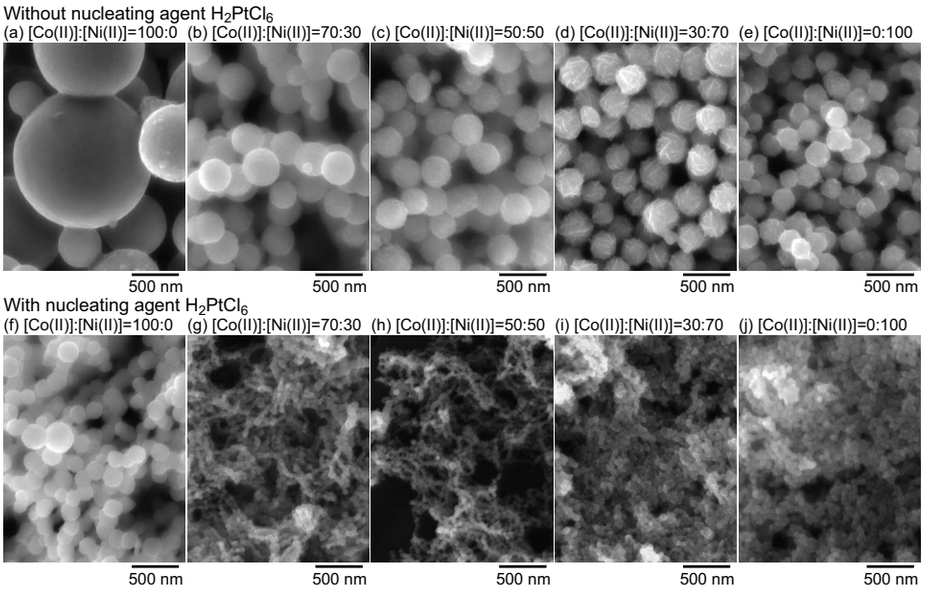

Figure 1. SEM images of particles synthesized from solutions containing (a) 0.050 M Co(II), (b) 0.035 M Co(II)–0.015 M Ni(II), (c) 0.025 M Co(II)–0.025 M Ni(II), (d) 0.015 M Co(II)–0.035 M Ni(II), and (e) 0.050 M Ni(II) in the absence of H_2PtCl_6, and (f) 0.050 M Co(II), (g) 0.035 M Co(II)–0.015 M Ni(II), (h) 0.025 M Co(II)–0.025 M Ni(II), (i) 0.015 M Co(II)–0.035 M Ni(II), and (j) 0.050 M Ni(II) in the presence of 1.0 mM H_2PtCl_6.

perimental runs by a potentiostat/galvanostat (Hokuto Denko Co., Ltd., HA-151) using a Ag/AgCl electrode (Horiba 2565A-10T) as a reference electrode. It was assumed that the measured immersion potential was almost the same as the mixed potential in the reaction suspension in this system, although the immersion of an electrode can affect the rates of partial redox reactions due to its catalytic activity. The cyclic voltammogram (CV) was also measured by the potentiostat/galvanostat using gold- or nickel-sputtered QCM substrates and a platinum electrode (20×20 mm) as the working and counter electrodes, respectively.

Results and Discussion

Figure 1 shows scanning electron microscopy (SEM) images of cobalt, nickel, and their alloy particles synthesized in EG, and Fig. 2 depicts the size distributions and mean diameters of the corresponding particles. The sparse agglomeration of particles can be seen under all conditions, which is due to magnetic interaction. In the absence of the nucleating agent H_2PtCl_6, the largest particles (922 nm in mean diameter) were obtained at $[Co(II)]:[Ni(II)] = 100:0$. The particle size gradually decreased with the increase in the composition of nickel in the particles, and the smallest particles (237 nm in mean diameter) were obtained at $[Co(II)]:[Ni(II)] = 0:100$. The increase in nickel amount also resulted in a sharp size distribution. Generally, nucleating agents such as H_2PtCl_6, whose redox potential is much higher than the objective metal, are utilized for the deposition of small metal particles. Small particles with a narrow size distribution were actually obtained by the addition of a minute amount of H_2PtCl_6 (1.0 mM) under all conditions. The addition of the nucleating agent also eliminated the dispersion of particle size distribution depending on its composition; particles approximately 50 nm in mean diameter were obtained except for the condition of $[Co(II)]:[Ni(II)] = 100:0$. Therefore, H_2PtCl_6 suitably works as a nucleating agent and provides the nucleation sites for cobalt, nickel, and their alloy particles. It can be presumed that the redox potentials of Co(II)/Co and Ni(II)/Ni are almost the same value in EG, and thus, the formation mechanism of small particles differs by the addition of nickel(II) salt or platinum(IV) salt. This difference is discussed later in detail.

The result of composition analysis with EDX is shown in Table I. The compositions of all the particles were almost the same as the concentration ratios of metallic ions in the reaction solution. This implies that the redox potential of the Co(II)/Co redox pair is very close to that of the Ni(II)/Ni redox pair. In addition, metal cobalt and nickel can be mixed at any concentration ratio, forming the face-

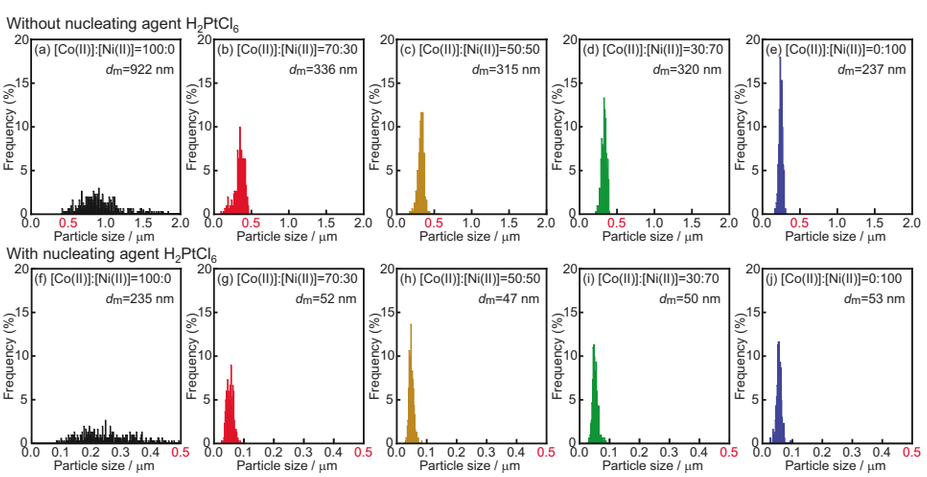

Figure 2. (Color online) Size distribution and mean diameter of particles synthesized from solutions containing (a) 0.050 M Co(II), (b) 0.035 M Co(II)–0.015 M Ni(II), (c) 0.025 M Co(II)–0.025 M Ni(II), (d) 0.015 M Co(II)–0.035 M Ni(II), and (e) 0.050 M Ni(II) in the absence of H_2PtCl_6, and (f) 0.050 M Co(II), (g) 0.035 M Co(II)–0.015 M Ni(II), (h) 0.025 M Co(II)–0.025 M Ni(II), (i) 0.015 M Co(II)–0.035 M Ni(II), and (j) 0.050 M Ni(II) in the presence of 1.0 mM H_2PtCl_6.

Table I. Composition of particles synthesized, changing the concentration ratio of Co(II) and Ni(II) in reaction solution.

	Concentration ratio in reaction solution [Co(II)]:[Ni(II)]:[Pt(IV)]	Co (atom %)	Ni (atom %)	Pt (atom %)
(a)	100:0:0	100.0	0.0	0.0
(b)	70:30:0	69.3	30.7	0.0
(c)	50:50:0	49.5	50.5	0.0
(d)	30:70:0	29.9	70.1	0.0
(e)	0:100:0	0.0	100.0	0.0
(f)	100:0:2	99.9	0.0	0.1
(g)	70:30:2	68.8	30.1	1.1
(h)	50:50:2	50.5	48.5	1.0
(i)	30:70:2	28.9	70.5	0.6
(j)	0:100:2	0.0	99.4	0.6

centered cubic (fcc) or hexagonal close-packed (hcp) structure, which allows the formation of Co–Ni nanoparticles with discretionary composition.

Figure 3 shows XRD patterns of the particles. As can be seen in the XRD patterns, only fcc nickel peaks are observed at the [Co(II)]:[Ni(II)] = 0:100 condition. In contrast, peaks due to both hcp and fcc cobalt are observed at [Co(II)]:[Ni(II)] = 100:0. Large fcc peaks and small hcp peaks are observed at [Co(II)]:[Ni(II)] = 70:30, 50:50, and 30:70. Overall, the strength of the hcp peaks is slightly larger in the presence of H_2PtCl_6 than in the absence of H_2PtCl_6, but the peak positions and peak widths of the XRD profiles are almost the same despite the presence or absence of H_2PtCl_6. According to the phase diagram of the Co–Ni alloy system, both the hcp and fcc Co–Ni alloys are stable (in equilibrium states) at [Co(II)]:[Ni(II)] = 70:30, whereas only the fcc Co–Ni alloy is most stable at [Co(II)]:[Ni(II)] = 50:50 and 30:70. It is not presently understood whether these particles involve independent hcp and fcc particles or whether one particle includes both the hcp and fcc phases at [Co(II)]:[Ni(II)] = 50:50 and 30:70. This can be confirmed by annealing; when one particle includes both the hcp and fcc phases, hcp grains must disappear by annealing. Figure 4 shows SEM images of the particles after annealing at 573 K in Ar atmosphere for 16 h. The spherical shape is still maintained after annealing, although the particles adhere a little to each other. The surface

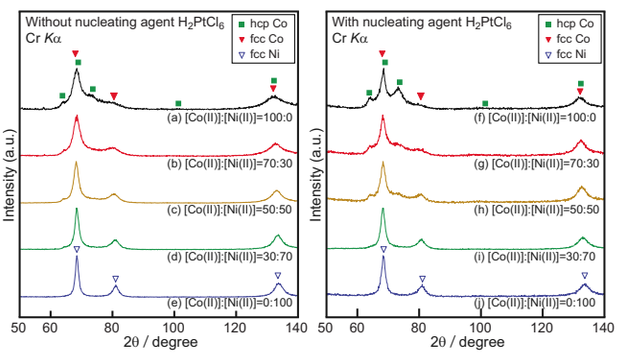

Figure 3. (Color online) XRD patterns of particles synthesized from solutions containing (a) 0.050 M Co(II), (b) 0.035 M Co(II)–0.015 M Ni(II), (c) 0.025 M Co(II)–0.025 M Ni(II), (d) 0.015 M Co(II)–0.035 M Ni(II), and (e) 0.050 M Ni(II) in the absence of H_2PtCl_6, and (f) 0.050 M Co(II), (g) 0.035 M Co(II)–0.015 M Ni(II), (h) 0.025 M Co(II)–0.025 M Ni(II), (i) 0.015 M Co(II)–0.035 M Ni(II), and (j) 0.050 M Ni(II) in the presence of 1.0 mM H_2PtCl_6.

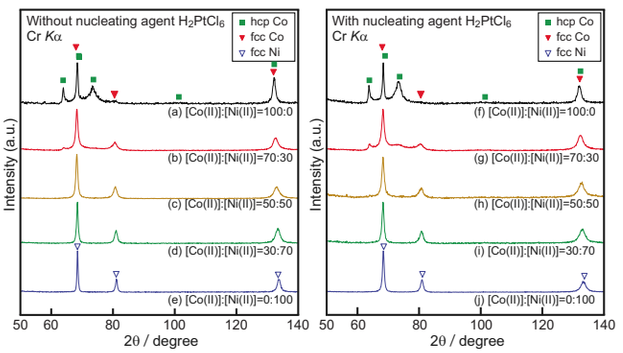

Figure 5. (Color online) XRD patterns of nanoparticles after annealing at 573 K in Ar atmosphere for 16 h synthesized from solutions containing (a) 0.050 M Co(II), (b) 0.035 M Co(II)–0.015 M Ni(II), (c) 0.025 M Co(II)–0.025 M Ni(II), (d) 0.015 M Co(II)–0.035 M Ni(II), and (e) 0.050 M Ni(II) in the absence of H_2PtCl_6, and (f) 0.050 M Co(II), (g) 0.035 M Co(II)–0.015 M Ni(II), (h) 0.025 M Co(II)–0.025 M Ni(II), (i) 0.015 M Co(II)–0.035 M Ni(II), and (j) 0.050 M Ni(II) in the presence of 1.0 mM H_2PtCl_6.

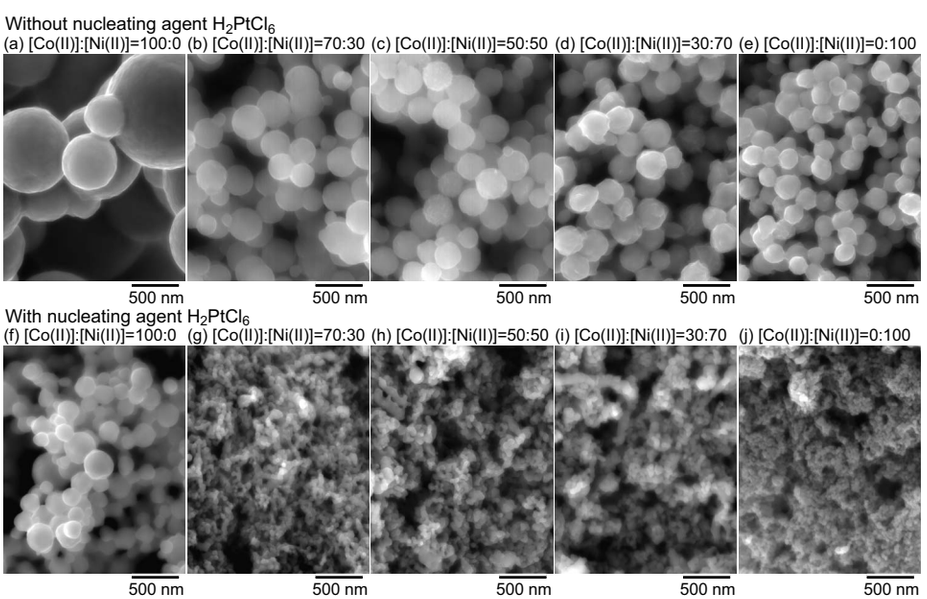

Figure 4. SEM images of nanoparticles after annealing at 573 K in Ar atmosphere for 16 h synthesized from solutions containing (a) 0.050 M Co(II), (b) 0.035 M Co(II)–0.015 M Ni(II), (c) 0.025 M Co(II)–0.025 M Ni(II), (d) 0.015 M Co(II)–0.035 M Ni(II), and (e) 0.050 M Ni(II) in the absence of H_2PtCl_6, and (f) 0.050 M Co(II), (g) 0.035 M Co(II)–0.015 M Ni(II), (h) 0.025 M Co(II)–0.025 M Ni(II), (i) 0.015 M Co(II)–0.035 M Ni(II), and (j) 0.050 M Ni(II) in the presence of 1.0 mM H_2PtCl_6.

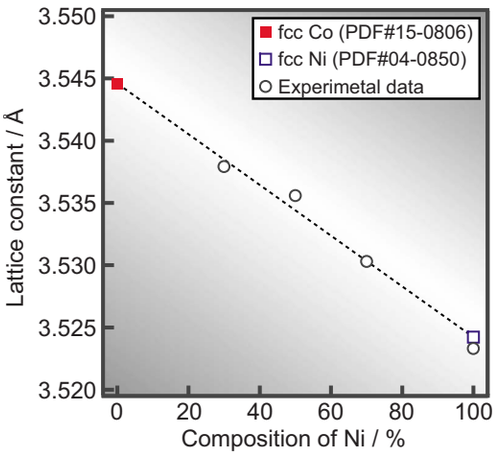

Figure 6. (Color online) Change in lattice constant of particles plotted with composition of Ni in the absence of nucleating agent H_2PtCl_6.

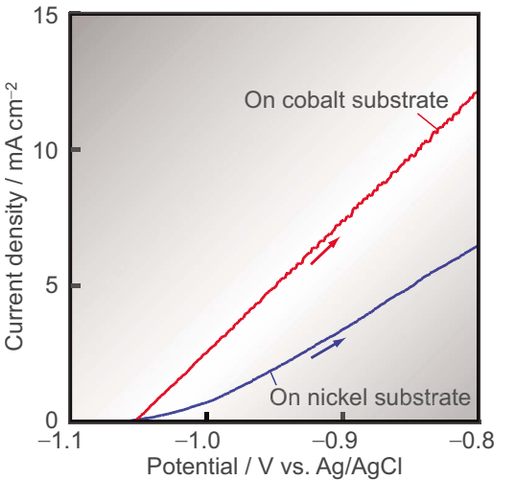

Figure 8. (Color online) Anodic polarization curves measured at 1 mV s^{-1} in EG containing 0.50 M N_2H_4 and 1.0 M NaOH on cobalt and nickel substrates. Initial potential is −1.1 V.

of the annealed particles is smoother than that of the unannealed particles. Corresponding XRD profiles are shown in Fig. 5. All the peaks are sharpened because of crystal growth. At [Co(II)]:[Ni(II)] = 50:50 and 30:70, the hcp peaks completely disappear after annealing, indicating that hcp and fcc phases originally coexisted in one particle. Figure 6 plots the lattice constants of the particles (without the nucleating agent) after annealing, calculated by the position of the fcc 200 peak at around $2\theta = 80°$. The lattice constant obeys Vegard's law; the lattice constant changes linearly between the two lattice constants of fcc cobalt and fcc nickel calculated from powder diffraction files (PDF no. 15-0806 and no. 04-0850).

Figure 7 depicts CVs measured by a potentiostat at 1 mV s^{-1} in 120 cm^3 of EG solution containing (a) 0.050 M $CoCl_2 \cdot 6H_2O$ and 1.0 M NaOH and (b) 0.050 M $NiCl_2 \cdot 6H_2O$ and 1.0 M NaOH. The cobalt or nickel chloride solution was hydrolyzed by adding 1.0 M NaOH to form cobalt or nickel hydroxide, which was dispersed in the EG solution. The gold-sputtered QCM substrate was used as a working electrode for (a) the cobalt reaction system, and the nickel-sputtered QCM substrate was used for (b) the nickel reaction system because nickel deposition was not observed at all on the gold-sputtered QCM substrate. The usual CV by a potentiostat includes all the information of redox reactions on the QCM substrate. However, the CV drawn from the weight change of the QCM substrate only contains information on metal deposition and dissolution. Comparing the CVs, the current density in the nickel reaction system is totally much lower than that in the cobalt reaction system. In the usual CV of the cobalt reaction system by a potentiostat, the cathodic current of hydrogen generation (reductive decomposition of water or EG) is observed below −1.04 V vs Ag/AgCl, which disturbs the observation of the cathodic current of cobalt deposition. The oxidization current of hydrogen adsorbed on the QCM substrate is observed above −1.04 V only in the anodic sweep. Similarly, in the usual CV of the nickel reaction system, the cathodic current of hydrogen generation is observed below −0.80 V. The oxidization current of hydrogen adsorbed on the QCM substrate is observed above about −0.80 V. In both cases, the cathodic current density is much higher than the anodic current density. This difference is mainly attributed to the amount of reactant; hydrogen is generated by the decomposition of EG, which is a solvent and is abundant in the reaction suspension. In contrast, hydrogen adsorbed on the QCM substrate is scarce. Moreover, cobalt and nickel easily form an oxide layer on its surface, preventing the anodic dissolution, which is another reason why the anodic current is small. In the CV of the cobalt reaction system by QCM, the cathodic current of cobalt deposition is seen below ca. −0.98 V during the cathodic sweep. Once cobalt completely covers the gold-sputtered QCM substrate, cobalt is deposited below ca. −0.85 V during the anodic sweep. Therefore, cobalt has a higher catalytic activity for cobalt deposition than gold, resulting in a small overpotential. Furthermore, there is also a possibility that the cobalt nucleation energy on cobalt is lower than that on gold, which is totally different from the underpotential deposition phenomenon of cobalt onto gold in aqueous solution.[19] Above −0.85 V, the anodic current of cobalt dissolution is observed up to −0.64 V. Thus, the redox potential of the Co(II)/Co redox pair can be determined to be approximately −0.85 V vs Ag/AgCl. In the

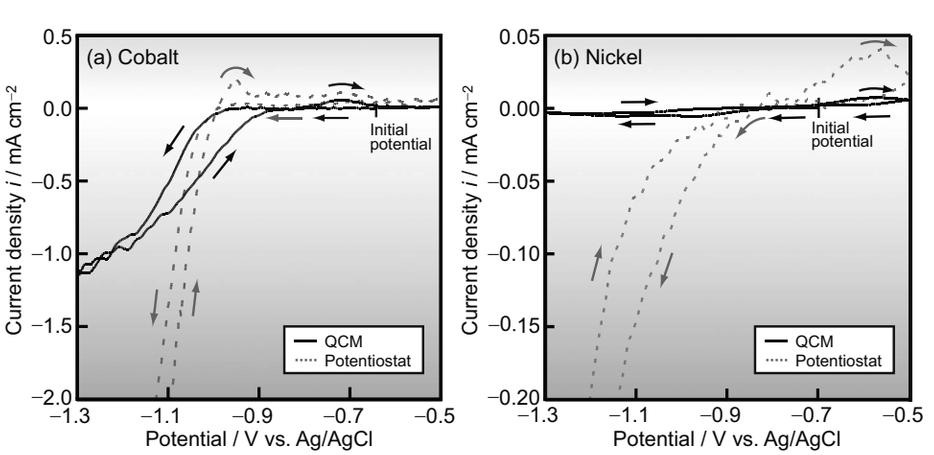

Figure 7. CVs measured by potentiostat (dotted line) and QCM (solid line) at 1 mV s^{-1} in EG containing (a) 0.050 M Co(II), 1.0 M NaOH and (b) 0.050 M Ni(II), 1.0 M NaOH. Initial potential is (a) −0.64 and (b) −0.70 V vs Ag/AgCl.

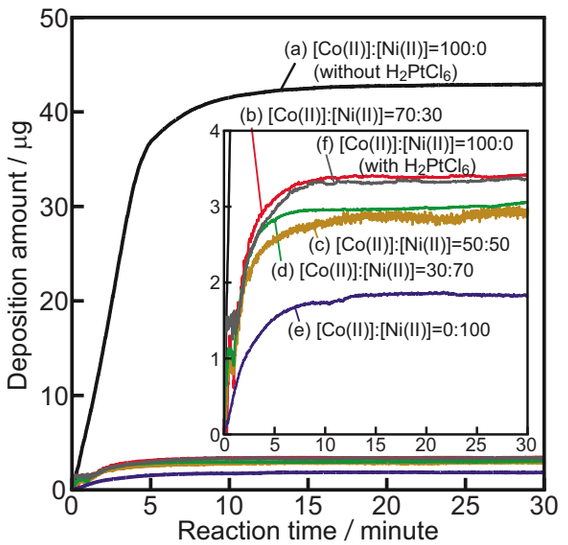

Figure 9. (Color online) Weight of metal deposited on gold-sputtered QCM substrate from solutions containing (a) 0.050 M Co(II), (b) 0.035 M Co(II)–0.015 M Ni(II), (c) 0.025 M Co(II)–0.025 M Ni(II), (d) 0.015 M Co(II)–0.035 M Ni(II), and (e) 0.050 M Ni(II) in the absence of H_2PtCl_6, and (f) 0.050 M Co(II) in the presence of H_2PtCl_6.

same way, the redox potential of the Ni(II)/Ni redox pair can be determined to be approximately −0.80 V vs Ag/AgCl from the CV of the nickel reaction system, which is nearly equal to the redox potential of the Co(II)/Co redox pair (c.a. −0.85 V). The current density of the CVs in the nickel reaction system is significantly smaller than those in the cobalt reaction system. Figure 8 shows anodic polarization curves measured in EG containing 0.50 M N_2H_4 and 1.0 M NaOH on cobalt and nickel substrates. The anodic current is observed around −1.05 V on both cobalt and nickel substrates, which corresponds mainly to hydrazine oxidation. Strictly, the current density is the sum of the current density of hydrazine oxidation (>0) and that of hydrogen generation (<0). The current density of the anodic polarization curve on the nickel substrate is also much smaller than that on the cobalt substrate. These results suggest that nickel has a much lower catalytic activity than cobalt for all the partial reactions, which agrees well with the results in different reaction systems by other researchers.[20,21] Therefore, metal deposition does not proceed so much on the nickel surface compared to the cobalt surface, and thus nucleation is preferable to particle growth in the nickel(II) solution. This is the reason why the size of nanoparticles decrease with increasing nickel amount.

Figure 9 shows the weight of metal deposited on the gold-sputtered QCM substrate during the reaction. The weight increases with time and the deposition finishes in 30 min. The total deposition amount corresponds to the inhomogeneous nucleation on the QCM substrate, which is inversely related to the nucleation in the reaction solution. With an increase in the amount of nickel(II) ions, the total deposition amount decreases, indicating that many nuclei are formed. Reliable QCM profiles were not obtained in the presence of the nucleating agent. This is because a very large number of nuclei were homogeneously formed in the reaction solution, and the deposition on the QCM substrate was infinitesimal.

Figure 10 shows the change with time in mixed potential in the reaction solution. Under all the conditions, the mixed potential was initially around −0.6 V vs Ag/AgCl and higher than the redox potentials of the Co(II)/Co and Ni(II)/Ni redox pairs, and rapidly dropped down below −1 V when the hydrazine solution was added. Subsequently, the mixed potential gradually increased with time, but the mixed potential was always below both the redox potentials of the Co(II)/Co and Ni(II)/Ni redox pairs, which indicates that metal deposition was possible during the reaction time. The potential change can be mainly attributed to the amount of hydrazine. Cobalt has a high catalytic activity for hydrazine oxidation reaction, and a large amount of hydrazine is consumed in solutions on the surface of particles with high compositions of cobalt. Therefore, the increased gradient of the mixed potential is steeper with increasing Co(II) amount except for the condition of [Co(II)]:[Ni(II)] = 100:0 in the absence of the nucleating agent. The catalytically active surface area increases with the decrease in particle size. In the present work, particle size decreases with increasing Ni(II) ion amounts in reaction solutions. At [Co(II)]:[Ni(II)] = 100:0, this size factor governs the consumption amount of hydrazine. Actually, in the presence of the nucleating agent, the size difference becomes small, and the consumption amount of hydrazine corresponds predominantly to the fraction of cobalt in the particles. Consequently, these two contradicting factors determine the consumption amount of hydrazine, and thus, the mixed potential.

Conclusion

In the present work, the synthesis process of Co–Ni alloy nanoparticles via electroless deposition in EG was electrochemically studied. We obtained the following results: Co–Ni alloy particles with almost the same composition as the concentration ratio of metallic ions in the reaction solution were obtained. This is because metal cobalt and nickel can be mixed at any concentration ratio. In addition, the redox potential of the Co(II)/Co redox pair is significantly close to that of the Ni(II)/Ni redox pair. Actually, the redox potentials of the Co(II)/Co and Ni(II)/Ni redox pairs in EG were experimentally determined to be almost the same (approximately −0.85 and −0.80 V vs Ag/AgCl, respectively), by using voltammetry combined with QCM. Cobalt has a high catalytic activity com-

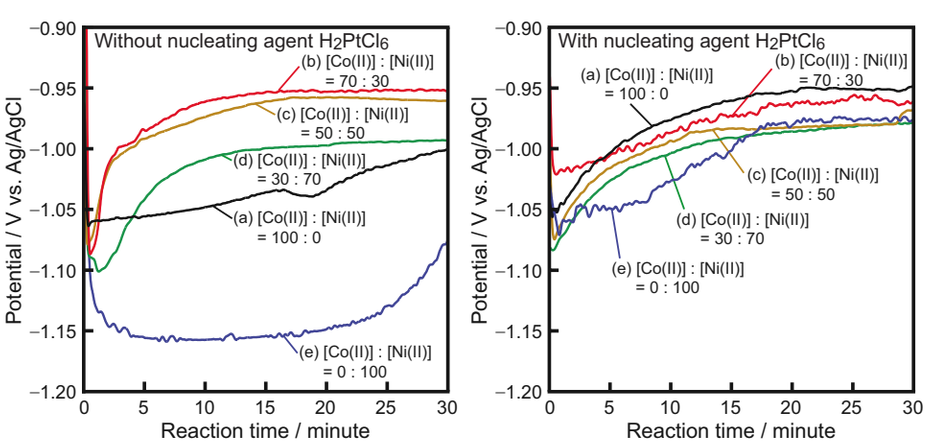

Figure 10. (Color online) Change in mixed potential in reaction solutions containing (a) 0.050 M Co(II), (b) 0.035 M Co(II)–0.015 M Ni(II), (c) 0.025 M Co(II)–0.025 M Ni(II), (d) 0.015 M Co(II)–0.035 M Ni(II), and (e) 0.050 M Ni(II) in the absence of H_2PtCl_6, and (f) 0.050 M Co(II), (g) 0.035 M Co(II)–0.015 M Ni(II), (h) 0.025 M Co(II)–0.025 M Ni(II), (i) 0.015 M Co(II)–0.035 M Ni(II), and (j) 0.050 M Ni(II) in the presence of 1.0 mM H_2PtCl_6.

pared to nickel for all the partial reactions, i.e., hydrazine oxidization, metal deposition, and hydrogen generation, resulting in decreasing particle size with increasing nickel amount. The mixed potential changes with time, which is mainly attributable to the remaining amount of hydrazine.

The method presented in this paper can be widely applied and helps us to thermodynamically consider even those systems where insufficient thermodynamic data are available.

Acknowledgments

This research was supported by a Grant-in-Aid for Knowledge Cluster Initiative (Kyoto Nanotechnology Cluster), Grant-in-Aid for the Global COE Program (International Center for Integrated Research and Advanced Education in Materials Science), and Grant-in-Aid for Young Scientists (B 20760505), all from the Japan Society for the Promotion of Science and Ministry of Education, Culture, Sports, Science and Technology of Japan. This research was also supported by the Kurata Memorial Hitachi Science and Technology Foundation and Shorai Foundation for Science and Technology.

Kyoto University assisted in meeting the publication costs of this article.

References

1. X. Li and S. Takahashi, *J. Magn. Magn. Mater.*, **214**, 195 (2000).
2. K. A. Tarasov, V. P. Isupov, B. B. Bakhonov, Y. A. Gapnov, B. P. Tolochko, M. M. Yulikov, A. Davidson, P. Beaunier, E. Marceau, and M. Che, *Microporous Mesoporous Mater.*, **107**, 202 (2008).
3. J. H. Kim and C. S. Yoon, *Thin Solid Films*, **516**, 4845 (2008).
4. R. Brayner, M.-J. Vaulay, F. Fiévet, and T. Coradin, *Chem. Mater.*, **19**, 1190 (2007).
5. G. Mattei, C. de Julián Fernández, P. Mazzoldi, C. Sada, G. De, G. Battaglin, C. Sangregorio, and D. Gatteschi, *Chem. Mater.*, **14**, 3440 (2002).
6. C. de Julián Fernández, C. Sangregorio, C. Innocenti, G. Mattei, and P. Mazzoldi, *Inorg. Chim. Acta*, **361**, 4138 (2008).
7. V. F. Meshcheryakov, Y. K. Fetisov, A. A. Stashkevich, and G. Viau, *J. Appl. Phys.*, **104**, 063910 (2008).
8. Y. M. Lee, C. W. Park, H. K. Choi, B. H. Koo, and C. G. Lee, *Met. Mater. Int.*, **14**, 117 (2008).
9. J. Vargas, C. Ramos, R. D. Zysler, and H. Romero, *Physica B*, **320**, 178 (2002).
10. Y. Li, C. Zhu, and C. Wang, *J. Phys. D*, **41**, 125303 (2008).
11. S. Yagi, H. Nakanishi, E. Matsubara, S. Matsubara, T. Ichitsubo, K. Hosoya, and Y. Matsuba, *J. Electrochem. Soc.*, **155**, D474 (2008).
12. S. Yagi, H. Nakanishi, T. Ichitsubo, and E. Matsubara, *J. Electrochem. Soc.*, **156**, D321 (2009).
13. M. D. L. Balela, S. Yagi, Z. Lockman, A. Aziz, A. V. Amorsolo, Jr., and E. Matsubara, *J. Electrochem. Soc.*, **156**, E139 (2009).
14. M. D. L. Balela, S. Yagi, and E. Matsubara, *Electrochem. Solid-State Lett.*, **13**, D4 (2010).
15. S. Yagi, T. Koyanagi, H. Nakanishi, T. Ichitsubo, and E. Matsubara, *J. Electrochem. Soc.*, **155**, D583 (2008).
16. S. Yagi, T. Nakagawa, E. Matsubara, S. Matsubara, S. Ogawa, and H. Tani, *Electrochem. Solid-State Lett.*, **11**, E25 (2008).
17. M. Pourbaix, *Atlas of Electrochemical Equilibria in Aqueous Solutions*, p. 384, Cebelcor, Brüssel (1966).
18. S. Yagi, M. Kawamori, and E. Matsubara, *Electrochem. Solid-State Lett.*, **13**, E1 (2010).
19. L. H. Mendoza-Huizar, J. Robles, and M. Palomar-Pardavé, *J. Electroanal. Chem.*, **521**, 95 (2002).
20. S. K. Singh, X.-B. Zhang, and Q. Xu, *J. Am. Chem. Soc.*, **131**, 9894 (2009).
21. B. H. Liu, Z. P. Li, and S. Suda, *J. Alloys Compd.*, **415**, 288 (2006).